Article | Open Access

Energy Materials

Zhao *et al. Energy Mater.* **2026**, *6*, 600113 **DOI:**10.20517/energymater.2026.163

Synergistic electrolyte engineering to enhance cycle stability of sodium ion batteries at high rates and elevated temperatures

Zhenyun Zhao[1,2,#], Tengda Wang[1,#], Zixiang Yang[2,#], Xu Wang[2], Yujia Cai[2], Wei Chen[1,*], Jianguo Lu[2,*]

Keywords:
Synergistic electrolyte engineering, layered transition metal oxides, sodium ion batteries, solid electrolyte interphase/cathode electrolyte interphase films, cycle stability, high-rate and elevated-temperature conditions

Citation: Zhao, Z.; Wang, T.; Yang, Z.; Wang, X.; Cai, Y.; Chen, W.; Lu, J. Synergistic electrolyte engineering to enhance cycle stability of sodium ion batteries at high rates and elevated temperatures. *Energy Mater.* **2026**, *6*, 600113. https://dx.doi.org/10.20517/energymater.2026.163

Received: 9 Jun 2026
First Decision: 25 Jun 2026
Revised: 13 Jul 2026
Accepted: 4 Aug 2026
Published: 8 Sep 2026

Academic Editor: Yuping Wu
Copy Editor: Fangling Lan
Production Editor: Fangling Lan

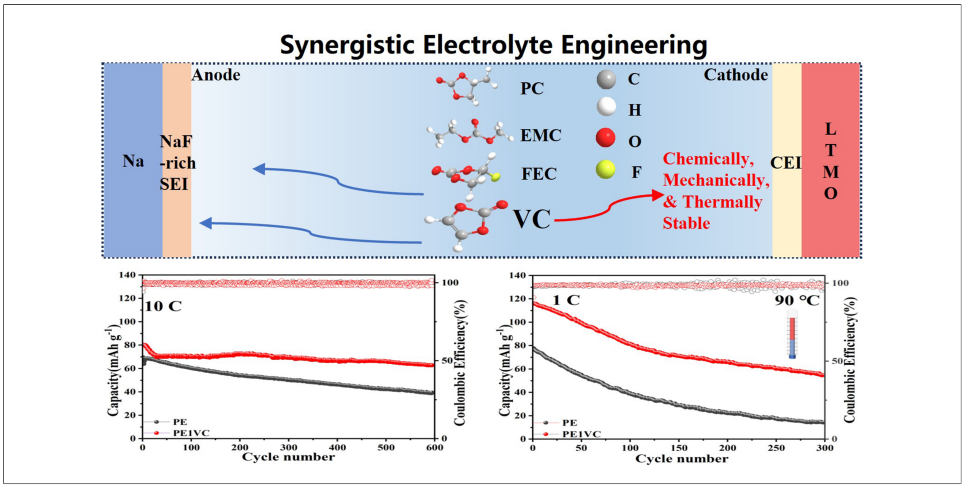

Abstract

Layered transition metal oxide (LTMO)-based sodium-ion batteries (SIBs) are prime candidates for outdoor stationary energy storage systems; however, their application is limited by rapid capacity decay under high-rate and elevated-temperature conditions. Herein, we propose a synergistic electrolyte engineering strategy based on a binary solvent system comprising propylene carbonate (PC) and ethyl methyl carbonate (EMC), supplemented with the film-forming electrolyte additives fluoroethylene carbonate (FEC) and vinylene carbonate (VC). The mixed electrolyte has been shown to enable the *in situ* formation of chemically stable, thermally resistant, and mechanically robust films on the LTMO cathode. The distinct functional roles of VC, FEC, PC, and EMC are systematically elucidated. Consequently, this synergistic electrolyte strategy enables LTMO-based SIBs to achieve outstanding cycle stability at high rates and elevated temperatures. Specifically, the LTMO-based SIBs delivered an initial capacity of 80 mAh g^{-1} at 10 C (from the long-term cycling test), retained 62.7 mAh g^{-1} after 600 cycles at 10 C, and retained 54.8 mAh g^{-1} after 300 cycles at 1 C at 90 °C. This study presents a scalable strategy for developing high-stability LTMO-based SIBs with strong adaptability to aggressive outdoor stationary

[1]National Engineering Lab for Textile Fiber Materials and Processing Technology, School of Materials Science and Engineering, Zhejiang Sci-Tech University, Hangzhou 310018, Zhejiang, China.
[2]State Key Laboratory of Silicon and Advanced Semiconductor Materials, School of Materials Science and Engineering, Zhejiang University, Hangzhou 310058, Zhejiang, China.
[#]Authors contributed equally.

[*]**Correspondence to:** Dr. Wei Chen, National Engineering Lab for Textile Fiber Materials and Processing Technology, School of Materials Science and Engineering, Zhejiang Sci-Tech University, Hangzhou 310018, Zhejiang, China. E-mail: wchen@zstu.edu.cn; Dr. Jianguo Lu,

State Key Laboratory of Silicon and Advanced Semiconductor Materials, School of Materials Science and Engineering, Zhejiang University, Hangzhou 310058, Zhejiang, China. E-mail: lujianguo@zju.edu.cn

energy storage environments.

INTRODUCTION

The global transition toward renewable energy has intensified the need for cost-effective, safe, and large-scale energy storage systems (ESSs)[1,2]. Sodium-ion batteries (SIBs) have emerged as a compelling alternative to lithium-ion batteries, largely due to the natural abundance and low cost of sodium resources[3,4]. Among various cathode candidates, layered transition-metal oxides (LTMOs, where TM = Mn, Fe, Ni, Co, Ti, V, *etc*.) have attracted particular attention for commercial applications due to their low cost and simplified synthesis routes[5,6]. However, the widespread adoption of LTMOs is hindered by rapid capacity loss during charge/discharge cycling, largely due to pronounced instability at the electrode-electrolyte interface[7,8].

To overcome this limitation, modifications to the bulk phase and the interfacial film have been widely reported, including elemental doping[9], cationic or anionic redox optimization[10], and artificial interfacial films (e.g., Al_2O_3 or $NaPO_3$)[11,12]. Besides, the electrolyte composition plays a decisive role in determining the interfacial stability of SIBs. A rational combination of solvents and functional additives in sodium electrolytes can not only facilitate ion transport but also enable *in situ* modulation of stable interfacial films on both sodium anodes and LTMO cathodes, thereby achieving excellent rate capability and cycling stability simultaneously[13,14].

Cyclic propylene carbonate (PC) is widely used as a baseline solvent in SIBs because of its high dielectric constant (64.4) and low cost, which together facilitate efficient salt dissociation and promote commercial viability. However, PC is prone to decomposition at the sodium anode, producing gases via an open-ring reaction[8]. To mitigate this issue, linear carbonates with complementary properties, such as ethylene carbonate (EC)[15], dimethyl carbonate (DMC)[16], and ethyl methyl carbonate (EMC)[17], are commonly used to form binary solvent systems. EMC has a low viscosity but a low dielectric constant. Therefore, combining PC and EMC can create a complementary solvent system that balances ionic dissociation and transport kinetics[18]. Moreover, forming robust interfacial films on both electrodes is essential for suppressing parasitic reactions. Fluoroethylene carbonate (FEC) is currently the most prevalent additive used to form a sodium fluoride (NaF)-rich solid electrolyte interphase (SEI) film on the sodium anode[19]. The cathode electrolyte interphase (CEI) film also requires careful regulation to further improve cycling stability. Various anhydride-based electrolyte additives have been reported to modify the CEI and suppress side reactions on LTMO cathodes[20]. Despite considerable efforts to modify the electrolytes of LTMO-based SIBs, their cycling stability at high rates and elevated temperatures remains inadequate, significantly limiting their applications in outdoor stationary conditions.

The energy and power densities of batteries depend on multiple electrolyte parameters, including viscosity, salt dissociation, ionic conductivity, and electrochemical window[21]. Cycle stability is closely tied to the electrode/electrolyte interfaces formed at both the anode and cathode[22]. Each solvent or additive has unique physicochemical properties, yet no single component can meet all design specifications. Thus, a synergistic electrolyte engineering approach that rationally combines solvents and additives is necessary. Under aggressive practical conditions, such as high rates and elevated temperatures, the CEI on LTMO cathodes tends to undergo chemical dissolution[23], mechanical fracture[24], and thermal decomposition[25]. Consequently, the LTMO cathodes are exposed to electrolyte solvents and attacked by decomposition byproducts. Hence, there is an urgent need to develop a synergistic electrolyte system capable of forming a

CEI film with high chemical, mechanical, and thermal robustness, thereby improving cycling stability at high rates and elevated temperatures.

In this work, we demonstrate that a mixed solvent of PC/EMC/FEC modified with vinylene carbonate (VC) effectively enhances the performance of a widely reported LTMO ($Na(NiFeMn)_{1/3}O_2$, NFM). By combining electrochemical impedance analysis, kinetic studies, and density functional theory (DFT) calculations, we confirmed the formation of a CEI film exhibiting high chemical, mechanical, and thermal robustness. This synergistic electrolyte engineering yields markedly improved cycling stability at high rates (5 C and 10 C) and at an elevated temperature (90 °C). Overall, this study presents a simple, scalable, and cost-effective strategy to optimize cycling stability at high rates and elevated temperatures, paving the way for the practical deployment of LTMO-based SIBs in grid-scale, industrial, and residential ESSs.

EXPERIMENTAL

Materials and agents

The study employs the following chemicals: Anhydrous sodium carbonate (Na_2CO_3, AR, Sinopharm Chemical Reagent Co. Ltd.), tannic acid (TA, $C_{76}H_{52}O_{46}$, 98%, Shanghai Macklin Biochemical Co. Ltd.), nickel-iron-manganese ternary hydroxide ($(NiFeMn)_{1/3}(OH)_2$, battery grade, Zhejiang Huayou Cobalt Co. Ltd.), polyvinylidene fluoride (PVDF, AR, Sinopharm Chemical Reagent Co. Ltd.), N-methyl-2-pyrrolidone (NMP, C_5H_9NO, AR, Shanghai Aladdin Biochemical Technology Co. Ltd.), anhydrous ethanol (AR, Sinopharm Chemical Reagent Co. Ltd.), VC ($C_3H_2O_3$, 99%, Shanghai Aladdin Biochemical Technology Co. Ltd.), conductive carbon black (C, battery grade, Timcal Graphite & Carbon), aluminum foil (battery grade, Shenzhen Tianchenghe), coin cell case (CR2032, Shenzhen Kejing Star), and glass fiber separator (GF/D, Whatman). All agents were used without further purification. The electrolyte consisted of sodium perchlorate ($NaClO_4$), a PC/EMC solvent mixture, and the FEC additive in a volume ratio of 50:48:2; it was purchased from Duoduo Chemical Technology Co. Ltd. and denoted as PE.

Preparation of O3-type $Na(NiFeMn)_{1/3}O_2$@CTA-4 electrode

The O3-type $Na(NiFeMn)_{1/3}O_2$@CTA-4 (NFM@CTA-4) was synthesized following our previously reported method[26]. The pristine O3-type NFM was prepared via high-temperature solid-state reaction. $(NiFeMn)_{1/3}(OH)_2$ and Na_2CO_3 were mixed in a molar ratio of 2:1.05. After grinding, the mixture was preheated at 500 °C for 3 h and then calcined at 900 °C for 12 h to obtain NFM. The as-obtained NFM was then ultrasonically dispersed in ethanol, followed by the addition of TA (4 wt%). The mixture was stirred at 80 °C until complete dissolution. The resulting solution was evaporated and dried under vacuum at 60 °C for 12 h. Finally, the product was calcined at 700 °C for 3 h under a nitrogen atmosphere (Kejing, OTF-1200X-II, China) to finish the carbon coating, yielding NFM@CTA-4. The electrodes were prepared by weighing the active material, conductive carbon black, and PVDF at a mass ratio of 8:1:1, using NMP as the solvent. Then, the suspension was cast onto aluminum foil using a doctor blade with a fixed gap of 100 μm, followed by vacuum drying at 80 °C for 12 h. The mass loading of NFM@CTA-4 on cathodes was around 2 mg cm^{-2}.

Preparation of electrolytes

Electrolyte preparation was carried out in an argon glovebox (MIKROUNA, Super, China, H_2O < 0.1 ppm, O_2 < 0.1 ppm). The PE electrolyte (10 mL) was mixed with VC additive at volume ratios of 99:1, 98:2, and 96:4, respectively. The mixtures were thoroughly shaken and allowed to stand until complete dissolution, yielding electrolytes denoted as PE1VC, PE2VC, and PE4VC, respectively.

Characterization and measurement

Scanning electron microscopy (SEM, ZEISS Sigma 360, GER) coupled with energy dispersive spectroscopy (EDS, OXFORD ULTIM MAX 100, UK) was used to characterize the microstructure of the samples. X-ray photoelectron spectroscopy (XPS, Thermo Scientific K-Alpha$^+$, USA) was used to characterize the

composition of CEI films. The CR2032 coin cells were assembled with a working electrode, sodium metal foil, glass fiber separator, and 100 μL electrolytes (PE, PE1VC, PE2VC, and PE4VC) in an argon glovebox (H_2O < 0.1 ppm, O_2 < 0.1 ppm). Two half-cells were assembled for each electrolyte, and the cell exhibiting the representative performance within each group was selected for subsequent evaluation. Galvanostatic charge-discharge curves (GCD), rate performance, and cycling stability were tested on a battery testing system (Neware, CT-4008Q, China). High-temperature testing was performed in a programmable temperature-controlled oven (Ruijia, DHG-9030A, China), calibrated to maintain temperature fluctuations within ±1 °C. Cyclic voltammetry (CV) and electrochemical impedance spectra (EIS) were tested by an electrochemical workstation (Chenhua, CHI690F, China). CV was performed over a voltage window of 2~4 V (*vs*. Na^+/Na) at scan rates ranging from 0.1 to 1 mV s^{-1}. EIS was recorded over a frequency range of 100 kHz to 0.01 Hz with an AC amplitude of 0.5 mV, and the obtained spectra were fitted by ZView software using a nonlinear least-squares method.

Theoretical calculations

The Gaussian 16 package was used to optimize the geometric structures of PC, EMC, FEC, and VC molecules. The values of the highest occupied molecular orbital (HOMO) and the lowest unoccupied molecular orbital (LUMO) energies were calculated using DFT with the B3LYP/6-311+G (d) functional/basis set. The electrostatic potential (ESP) maps were obtained by further calculating on Gaussian checkpoint files.

RESULT AND DISCUSSION

Theoretical calculation and SEI characterization

LTMOs for SIBs commonly suffer from severe interfacial side reactions. Carbon coating modification and electrolyte engineering are effective strategies to suppress these detrimental reactions. In our previous work, a carbon-coated NFM@CTA-4 cathode was synthesized, delivering 108.6 mAh g^{-1} at 1 C, with a capacity retention of 73.5% after 300 cycles[26]. In this study, we utilize the previously reported high-performance NFM@CTA-4 as the cathode and propose a synergistic electrolyte engineering strategy to further enhance the cycling stability of LTMO-based SIBs.

To predict the binding sites of Na^+ with electrolyte solvents/additives at the molecular level, the ESP distributions of PC, EMC, FEC, and VC were simulated. Positively charged Na^+ preferentially bind to the negatively charged sites of solvents/additives. As shown in Figure 1A, all four molecules exhibit the most negative ESP values around the C=O groups, indicating that Na^+ ions primarily coordinate with solvents/additives via these groups. Subsequently, the binding energies of Na^+ with the electrolyte components were calculated. The binding energy between a solvent and Na^+ reflects the strength of their coordination. Higher coordination strength facilitates the dissociation of $NaClO_4$ salt and the formation of solvated structures; however, it can conversely hinder desolvation at the electrode-electrolyte interface. As shown in Figure 1B, the binding energy between PC and Na^+ is -139.9 kJ mol^{-1}, indicating stronger coordination with Na^+. However, this also results in a higher desolvation energy barrier, which is unfavorable for rate capability. In contrast, the binding energy between EMC and Na^+ is -110.9 kJ mol^{-1}, indicating weaker coordination with Na^+. As a result, the solvation structure loosens, reducing the Na^+ desolvation energy. Therefore, the combination of PC and EMC can enhance the rate capability by modulating the overall coordination strength. Meanwhile, the binding energies of VC (-115.8 kJ mol^{-1}) and FEC (-120.6 kJ mol^{-1}) fall between those of PC and EMC, striking an optimal balance that facilitates both salt dissociation and interfacial desolvation.

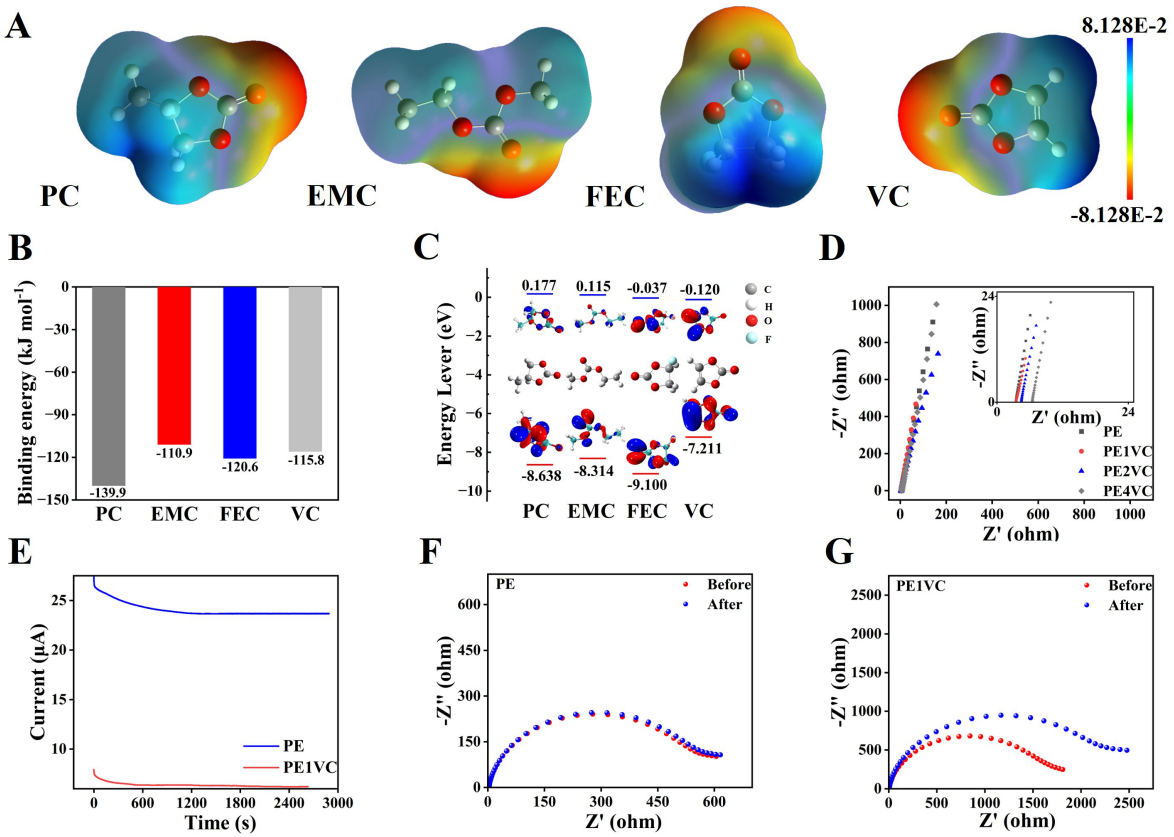

Figure 1. (A) ESP image of PC, EMC, FEC and VC; (B) Binding energies of PC, EMC, FEC and VC with Na^+; (C) HOMO and LUMO energy levels of PC, EMC, FEC and VC; (D) EIS of four electrolytes, with the enlarged view in the inset; (E) Chronoamperometric curves of the Na||Na cells with PE and PE1VC electrolytes, respectively; (F and G) EIS of the Na||Na cells before and after the chronoamperometric test with PE and PE1VC electrolytes, respectively.

To assess the rationale for using FEC and VC as film-forming electrolyte additives, the HOMO and LUMO energy levels of the electrolyte components were calculated, and the results are shown in Figure 1C. These frontier orbitals govern the redox reactivity of electrolyte components, thereby determining the formation of SEI and CEI films[27]. The SEI and CEI are critical to the capacity, rate capability, and cycling stability of sodium anodes and LTMOs, respectively, and thus dictate the performance of half-cells. FEC, with a low LUMO energy level (-0.037 eV), preferentially undergoes reduction to form a NaF-rich SEI that effectively passivates the sodium anode. Meanwhile, among the four components, VC exhibits both the lowest LUMO energy level (-0.120 eV) and the highest HOMO energy level (-7.211 eV). Therefore, it can be preferentially oxidized and reduced during electrochemical reactions, promoting the formation of both SEI and CEI films that protect the anodes and cathodes from corrosion caused by electrolyte decomposition byproducts.

To investigate interfacial charge transfer, EIS measurements were conducted on Na||Na symmetric cells. From the EIS spectra in Figure 1D and the inset, the electrolyte resistances (R_e) were determined from the high-frequency intercept on the Z' axis. Notably, compared with PE2VC and PE4VC, PE and PE1VC exhibit lower R_e values, indicating lower bulk electrolyte resistance. The Na||Na symmetric cells using PE2VC and PE4VC electrolytes exhibit higher R_e than those using PE and PE1VC electrolytes. The elevated R_e observed for PE2VC and PE4VC is attributed to the electrically insulating nature of VC. To further elucidate the influence of the VC additive on Na^+ transport, the Na^+ transference numbers of PE and PE1VC were subsequently calculated via the chronoamperometric curves [Figure 1E], as well as the EIS before and after the chronoamperometric test [Figure 1F and G]. The Na^+ transference number was calculated using:

$$t_{Na^+} = \frac{I_{SS}(\Delta V - I_0 R_0)}{I_0(\Delta V - I_{SS} R_{SS})} \quad (1)$$

where ΔV is the applied polarization voltage (20 mV), I_0 and I_{SS} are the initial and steady-state currents, respectively, and R_0 and R_{SS} are the initial and steady-state resistances of the passivation films on the Na electrode, respectively[28]. The resistance values were determined from the diameters of the semicircles in Figure 1F and G. The Na^+ transference numbers were calculated to be 0.63 for PE and 0.90 for PE1VC. Furthermore, a high Na^+ transference number can effectively suppress concentration polarization, thereby enhancing rate capability. These results indicate that PE1VC strikes an optimal balance between bulk ionic conductivity and the Na^+ transference number.

To gain further insight into electrolyte properties, electrochemical measurements were conducted on Na||Na symmetric cells with PE and PE1VC electrolytes at a current density of 2 mA cm^{-2} [Supplementary Figures 1 and 2]. The voltage-time profiles show that the symmetric cell with the PE electrolyte has a lower overpotential during the initial 30 h. However, after 30 h of cycling, the overpotential of the PE-based cell continues to increase, whereas that of the PE1VC-based cell gradually decreases and eventually stabilizes. This result confirms that the preferential decomposition of the VC additive facilitates the formation of a stable SEI film that effectively protects the Na anode while enabling efficient Na^+ transport. In contrast, the PE electrolyte undergoes continuous decomposition, resulting in excessive SEI thickening that ultimately impedes Na^+ transport.

Electrochemical performance

To clarify the influence of the VC additive on the electrochemical Na^+ storage performance, GCD tests were conducted at various current rates using half-cells assembled with four distinct electrolytes: PE, PE1VC, PE2VC, and PE4VC. As shown in Figure 2A-D, the charge profiles of all four samples at 1 C display a dominant plateau at around 3.3 V, corresponding to the Ni^{2+}/Ni^{3+} oxidation. The discharge profile consists primarily of a plateau near 2.5 V, which is associated with a two-phase transition reaction, and a sloping region near 3.0 to 4.0 V attributable to a solid-solution reaction. A sudden voltage surge was observed at the beginning of charging at 5 C. This surge is attributed to the superposition of instantaneous ohmic and activation polarizations induced by the abrupt transition from low-rate to high-rate operation. Specifically, the current step induces an immediate voltage jump governed by ohmic resistance, while the electrode interfaces require additional overpotential to drive the suddenly accelerated electrochemical reaction kinetics at high current[29].

As shown in Figure 2E, the cell with the PE1VC electrolyte delivers an initial discharge specific capacity of 120.2 mAh g^{-1} at 1 C (1 C = 150 mA g^{-1}), whereas those with PE, PE2VC, and PE4VC electrolytes deliver 115.8, 120.1, and 116.8 mAh g^{-1}, respectively. Moreover, PE1VC exhibits superior rate capability at high rates, delivering the highest discharge specific capacities of 89.8 mAh g^{-1} at 5 C and 68.9 mAh g^{-1} at 10 C. This behavior can be attributed to the rapid formation of a stable SEI film with a high Na^+ transference number, which ensures fast Na^+ transport kinetics and excellent stability (discussed above). In addition, VC facilitates the formation of a thermally stable and mechanically robust CEI film, which protects the cathode from corrosion (discussed later).

As shown in Figure 2F, the Coulombic efficiencies of all four samples are nearly 100%. After 300 cycles at 1 C, the retained capacities of the PE, PE1VC, PE2VC, and PE4VC cells are 74.9, 84.8, 83.5, and 79.8 mAh g^{-1}, respectively, indicating that PE1VC provides significantly improved cycling stability. To further assess durability, all four samples were subjected to 600 GCD cycles at 10 C. As shown in Figure 2G, after 600 cycles, PE1VC exhibits the highest reversible capacity (62.7 mAh g^{-1}) and the best capacity retention (78.4%),

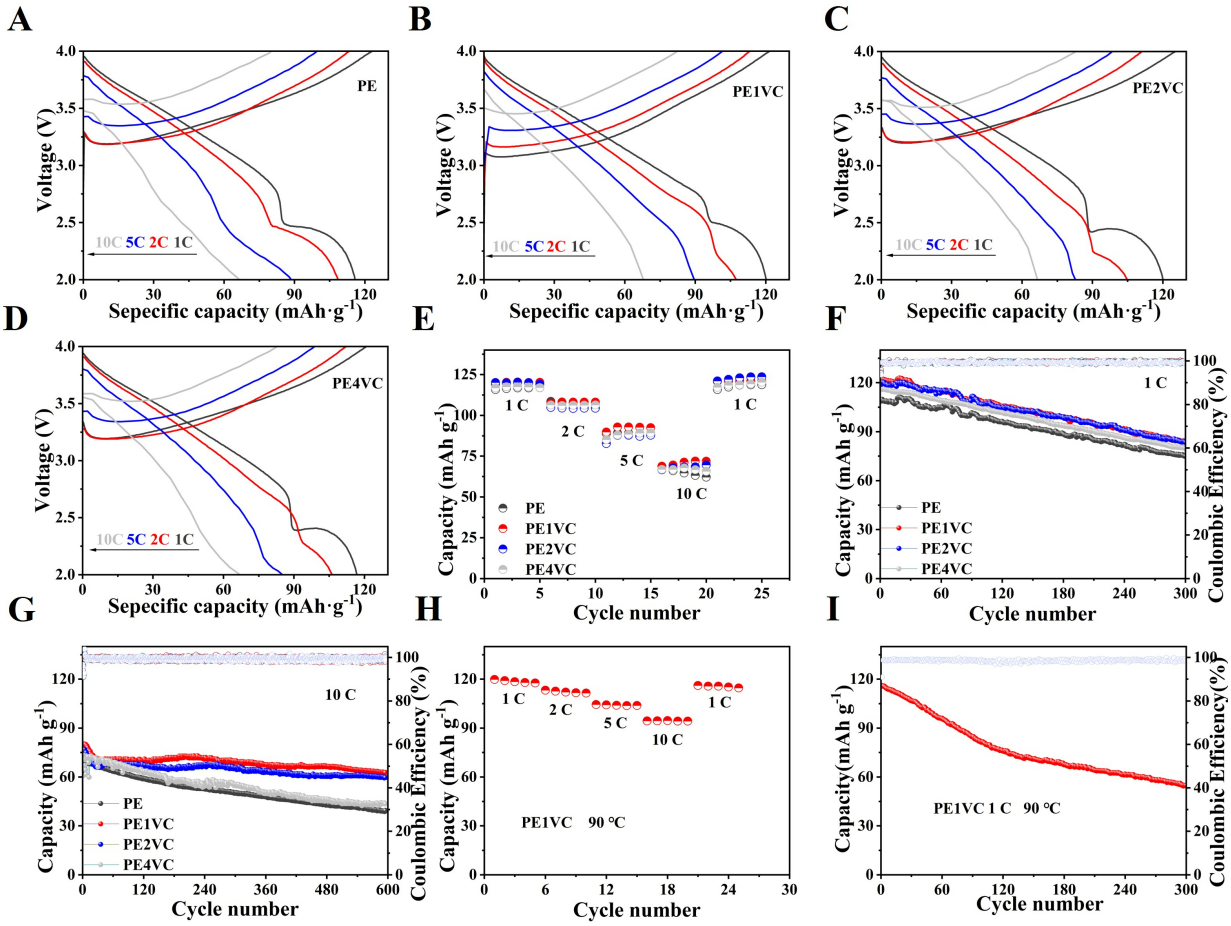

Figure 2. GCD of half-cells with (A) PE, (B) PE1VC, (C) PE2VC and (D) PE4VC electrolytes at different rates; (E) Rate capability of the NFM@CTA-4||Na half-cells with the four electrolytes; Cycling performance of the NFM@CTA-4||Na half-cells with the four electrolytes at (F) 1 C and (G) 10 C; (H) Rate capability and (I) Cycling performance of the NFM@CTA-4||Na half-cells with PE1VC at 90 °C. Solid spheres indicate cycling capacity and hollow spheres indicate Coulombic efficiency.

outperforming PE (39.4 mAh g^{-1}, 56.5%), PE2VC (59.7 mAh g^{-1}, 77.7%), and PE4VC (43.5 mAh g^{-1}, 71.5%). Notably, all VC-containing electrolytes exhibit superior capacity retention compared with PE.

To evaluate electrochemical performance at elevated temperatures, rate capability and cycling stability were evaluated at 90 °C. As shown in Figure 2H, PE1VC delivers high specific capacities of 104.48 mAh g^{-1} at 5 C and 94.4 mAh g^{-1} at 10 C. The enhanced capacities at 90 °C, compared with those at 25 °C, result from reduced electrolyte viscosity, improved sodium salt dissociation, and accelerated electrode kinetics. Although the rate capability is enhanced, the elevated temperature simultaneously accelerates side reactions and structural degradation of the electrode material, thereby compromising cycling stability. After 300 cycles at 90 °C, the discharge specific capacity of PE1VC drops to 54.8 mAh g^{-1}, corresponding to a capacity retention of 47.24% [Figure 2I]. In contrast, PE exhibits much poorer cycling stability under the same conditions, retaining only 14.5 mAh g^{-1} (18.68% retention) [Supplementary Figure 3]. Additionally, the button cells with PE and PE1VC electrolytes exhibited no pressure-induced rupture during or after cycling at 90 °C and retained their original structural integrity.

The boiling point of VC (162 °C) lies between those of PC (241.7 °C) and EMC (109 °C). Owing to its relatively high boiling point, VC remains thermally stable at typical operating temperatures (≤ 90 °C), thereby ensuring sustained electrochemical performance[30]. Furthermore, among the electrolyte components,

VC exhibits the lowest LUMO energy level and the highest HOMO energy level, indicating its thermodynamic tendency to undergo preferential reduction at the anode and preferential oxidation at the cathode. Thus, the VC additive contributes to the rapid formation of SEI films on the Na foils and CEI films on the cathodes. Specifically, during charging, it facilitates cleavage of the C=C bond and the subsequent ring-opening reactions of VC, leading to the formation of poly-VC and other oligomeric/polymeric species that constitute the CEI. These species coalesce into a protective film on the cathode surface, thereby effectively shielding the NFM@CTA-4 active material from corrosive byproducts generated during electrolyte decomposition[31-33]. Besides, CEI and SEI films formed in the presence of VC usually exhibit enhanced thermal stability[34,35].

The enhanced cycling stability observed at room temperature, at high rates, and at 90 °C is attributed to the rapid formation of stable SEI films on Na foils and CEI films on NFM@CTA-4 cathodes, enabled by the VC additive. On the one hand, VC exhibits the lowest LUMO energy level among the mixed electrolytes, so it can be preferentially reduced, thereby facilitating the formation of a robust, ionically conductive SEI film. On the other hand, VC possesses a higher HOMO energy level than the others (FEC, PC, EMC), facilitating its preferential oxidation at the cathode interface and driving the *in situ* formation of a CEI film that combines chemical inertness, thermal resilience, and mechanical integrity with fast Na^+ transport kinetics. The CEI film can protect cathodes from electrolyte-induced corrosion, mitigate side reactions, and suppress cracking and pulverization, as will be discussed later.

Electrochemical kinetics

To investigate electrode redox reactions, CV measurements were conducted on NFM@CTA-4 cathodes with PE, PE1VC, PE2VC, and PE4VC electrolytes. The CV profiles of the first three cycles are shown in Figure 3A and B (PE and PE1VC) and Supplementary Figures 4 and 5 (PE2VC and PE4VC). The Ni^{3+}/Ni^{2+} redox couple is considered the primary contributor to capacity in NFM-type cathode materials. The redox peaks observed at 2.8/3.3 V (Peak C/A) are predominantly assigned to the Ni^{2+}/Ni^{3+} couple, whereas the peaks at around 3.55/3.6 V (Peak D/E) are widely ascribed to the Fe^{3+}/Fe^{4+} redox couple[31,36]. The reduction peak at 2.5 V (Peak B) is tentatively attributed to the partial reduction of Mn^{4+} to Mn^{3+} during the initial charge/discharge cycles[37].

To further elucidate the electrode reaction kinetics in the presence of the VC additive, CV curves were recorded at scan rates ranging from 0.1~1 mV s^{-1}. As shown in Figure 3C and D (PE and PE1VC) and Supplementary Figures 6 and 7 (PE2VC and PE4VC), the peak current increases monotonically with increasing scan rate. Notably, the CV profiles of the bare PE electrolyte exhibit pronounced peak distortions, whereas those of the VC-containing electrolytes show minimal scan-rate dependence, which is attributable primarily to the formation of a robust CEI film induced by the VC additive. The reaction kinetics can be quantitatively assessed through the power-law formula given in:

$$i = av^b \tag{2}$$

$$\log i = b \log v + \log a \tag{3}$$

Where i is the peak current and v is the scan rate. The b-value was extracted from the slope of the log i versus log v plot via least-squares linear regression. The value of b provides insight into the charge-storage mechanism: $b \approx 0.5$ indicates diffusion-controlled behavior, while $b \approx 1$ suggests adsorption-controlled behavior[38]. Based on the peak currents in Figure 3C and D, the b-values of the four peaks are calculated to be 0.98, 0.71, 0.59, and 0.96 for PE, and 0.97, 0.85, 0.67, and 0.96 for PE1VC, respectively [Figure 3E and F]. Most b-values are close to 1, indicating that adsorption-controlled charge-transfer processes dominate the

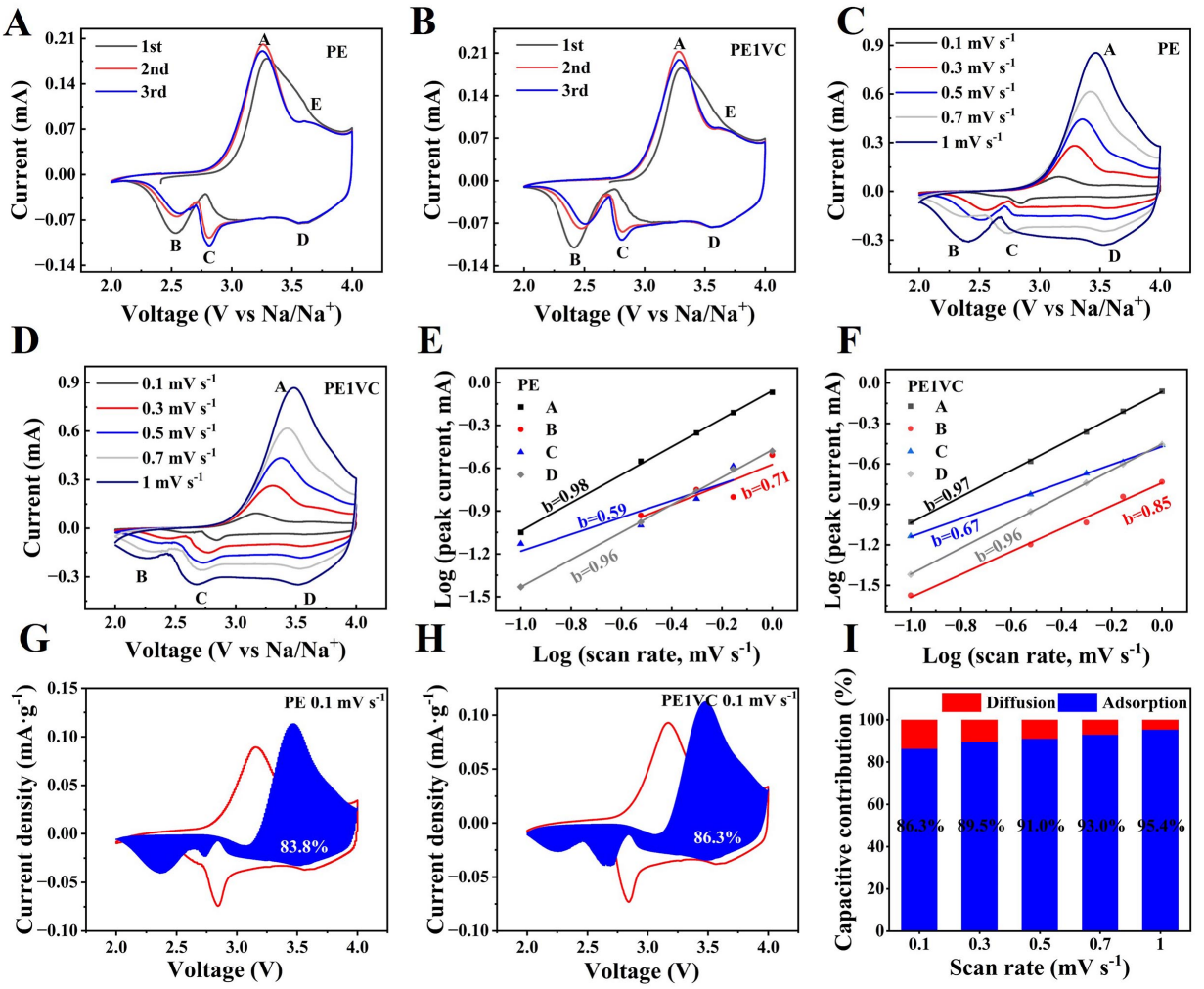

Figure 3. CV profiles of the first three cycles of the half-cells with (A) PE and (B) PE1VC electrolytes at 0.2 mV s^{-1}; CV curves of the half-cells with (C) PE and (D) PE1VC electrolytes at different scanning rates from 0.1 to 1 mV s^{-1}; Plots of log (*i*) vs. log (*v*) of the half-cells with (E) PE and (F) PE1VC electrolytes; CV curves of the half-cells with (G) PE and (H) PE1VC at 0.1 mV s^{-1} with the adsorption-controlled part highlighted in blue; (I) Adsorption and diffusion contributions of the half-cell with PE1VC.

electrode reactions. Notably, the PE1VC electrolyte exhibits relatively higher *b*-values (averaging 0.86) than PE, PE2VC, and PE4VC [Supplementary Figures 8 and 9], suggesting faster Na^+ transfer under high-rate and high-capacity conditions at high current. This observation is consistent with the superior rate stability of PE1VC. This trend also indicates that PE and PE1VC electrolytes promote faster redox reaction kinetics. The relatively sluggish reaction kinetics observed for PE2VC and PE4VC arise primarily from the electrically insulating nature of VC. An additional contributing factor is their higher charge transfer resistance (R_{ct}) compared to those of PE and PE1VC, as quantified by EIS and discussed later.

Based on the CV profiles, the adsorption-controlled contribution (k_1v) and the diffusion-controlled contribution ($k_2v^{1/2}$) for PE and PE1VC were quantitatively determined using:

$$i = k_1v + k_2v^{1/2} \quad (4)$$

Where *i* is the current at a given potential V, *v* is the scan rate, k_1v is the current component from the adsorption contribution, and $k_2v^{1/2}$ is the current component from the diffusion contribution[39]. Consequently, the adsorption-controlled current component ($i_{surf} = k_1v$) was determined at each potential

point. The total capacitive contribution (represented by the blue-shaded area in Figure 3G and H) was then quantified by integrating i_{surf} across the voltage window and normalizing it against the total charge of the measured CV curve. At a scan rate of 0.1 mV s^{-1}, the adsorption-controlled contributions are 83.84% for PE and 86.25% for PE1VC. As shown in Figure 3I, the adsorption-controlled contributions of PE1VC are 86.3%, 89.5%, 91.0%, 93.0%, and 95.4% as the scan rate rises from 0.1 to 1 mV s^{-1}, whereas those of PE show a fluctuating trend [Supplementary Figure 10]. The consistently high and progressively increasing adsorption-controlled contribution observed for PE1VC indicates that the VC additive promotes Na^+ transport kinetics and improves electrochemical reversibility. This is a major reason for the good rate capability and cycling stability.

EIS analysis and surface characterization

To further investigate the influence of the VC additive on CEI film formation, EIS was conducted on NFM@CTA-4||Na half-cells assembled with the four electrolytes [Figure 4A-D]. The simulated impedance spectra exhibit excellent agreement with the experimental EIS data, validating the proposed equivalent circuit model [Supplementary Figure 11]. The corresponding extracted impedances under different conditions are listed in Table 1. The electrolyte resistance (R_e) values of PE, PE1VC, PE2VC, and PE4VC remained similar across different tested conditions (the pristine state, after 3 cycles at 1 C, after 300 cycles at 1 C, and after 600 cycles at 10 C). The surface film resistance (R_{sf}) of the cell with the PE electrolyte increased markedly from 760.3 to 4,884 Ω after 3 cycles at 1 C, and then decreased to 948 Ω after 300 cycles. This is likely attributed to the initial formation and subsequent decomposition of an unstable CEI. Although its R_{ct} decreased continuously, remarkable capacity decays were observed during charge-discharge cycling, reflecting that the evolving structure facilitates charge transfer yet compromises Na^+ storage capacity mainly due to irreversible structural reconstructions within the electrode[40]. In contrast, the incorporation of VC fundamentally alters the interfacial evolution. All VC-containing systems display a progressive increase in R_{sf} during cycling at 1 C up to 300 cycles, yet the growth rate is highly concentration-dependent. Specifically, for the cell with PE1VC, R_{sf} increased slightly from 2,312 to 2,950 Ω after 3 cycles at 1 C and remained relatively stable over 300 cycles, while R_{ct} decreased from 69,817 to 18,229 Ω after 3 cycles and remained nearly unchanged thereafter. The initial decrease is attributed to interfacial activation[41]. After that, the almost unchanged R_{ct} indicates that an optimal amount of VC promotes the formation of a stable and highly ionically conductive CEI film on the cathode, thereby resulting in significantly smaller impedance changes during cycling with PE1VC than with PE. By comparison, the cells with PE2VC and PE4VC electrolytes also exhibited an initial decrease in R_{ct} after 3 cycles but showed a progressive increase after 300 cycles. This demonstrates that excessive VC triggers over-polymerization within the CEI, thereby hindering Na^+ transport kinetics and underscoring the critical trade-off between interfacial passivation and ionic conductivity. Notably, EIS measurements of the four half-cells after 600 cycles at a high rate of 10 C [Figure 4D] reveal substantially lower R_{ct} and R_{sf} values compared to those recorded after 300 cycles at 1 C [Figure 4C and Table 1]. This demonstrates that the NFM@CTA-4 cathode material, paired with the PC/EMC/FEC-based electrolyte, exhibits superior interfacial kinetics and stability under high-rate operation, consistent with its excellent rate capability and markedly enhanced cycling stability at 10 C relative to 1 C [Figure 2E-G].

To elucidate the role of VC in modulating the composition and interfacial stability of the CEI on the NFM@CTA-4 cathode, XPS analysis was performed on the cathode sample in PE1VC cycled for 3 cycles at 1 C. As shown in Figure 4E, the F 1s spectrum exhibits two peaks located at 684.8 eV (Na-F), and 688.1 eV (C-F), which indicate NaF is an important component of the CEI film[32,42]. In the C 1s spectrum [Figure 4F], the main oxygen containing contributions are observed at 285.4 eV (C-O) and 288.8 eV (C=O), consistent with the polyether-type backbone generated via the ring-opening polymerization of VC[31]. This is further supported by the O 1s spectrum [Supplementary Figure 12], where the intense peaks at 531.7/533.4 eV correspond to C=O/C-O species. No evident shift or emergence of new features is observed in the Mn 2p

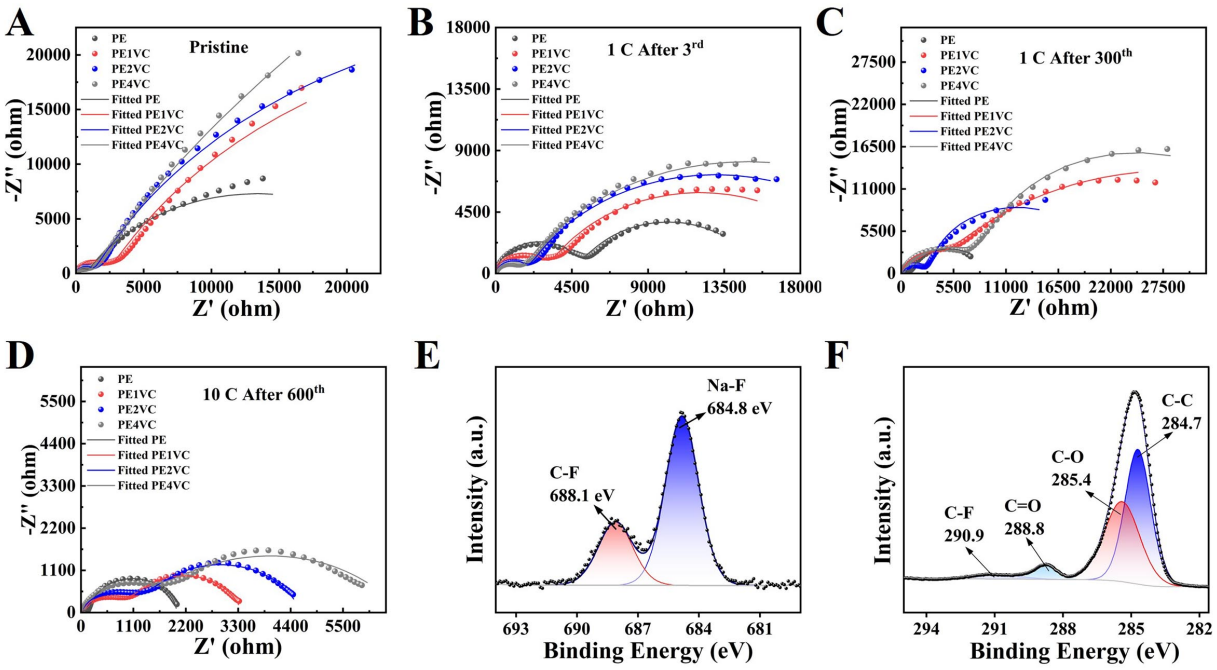

Figure 4. EIS and fitting curves of the half-cells with four electrolytes at different tested conditions, including (A) pristine state, (B) after 3 cycles at 1 C, (C) after 300 cycles at 1 C, and (D) after 600 cycles at 10 C; XPS high-resolution spectra of (E) F 1s and (F) C 1s of the NFM@CTA-4 cathode cycled in PE1VC for 3 cycles at 1 C.

Table 1. EIS fitting data of four samples at different tested conditions (the pristine state, after 3 cycles at 1 C, after 300 cycles at 1 C, and after 600 cycles at 10 C)

		PE (Ω)	PE1VC (Ω)	PE2VC (Ω)	PE4VC (Ω)
	R_e	3.41	3.65	3.38	4.836
Pristine	R_{sf}	760.3	2,312	1,207	970.7
	R_{ct}	25,275	69,817	72,872	181,460
1 C After	R_e	3.90	3.89	6.07	3.78
3rd	R_{sf}	4,884	2,950	1,805	1,417
	R_{ct}	10,642	18,229	22,408	26,893
1 C After	R_e	6.58	6.04	4.99	4.85
300th	R_{sf}	948	3,198	8,981	2,989
	R_{ct}	8,195	18,063	32,013	51,262
10 C After	R_e	4.44	5.19	5.20	5.74
600th	R_{sf}	184.1	1,060	1,369	1,393
	R_{ct}	1819	2,302	3,236	5,417

spectrum upon cycling compared with that of the pristine NFM@CTA-4 powder (as reported in our previous work[26] and shown in [Supplementary Figure 13], demonstrating minimal transition-metal dissolution and passivating capability of the CEI film. Collectively, these results demonstrate that VC functions as an effective electrolyte additive, facilitating the *in situ* formation of a chemically stable CEI.

To directly visualize the impact of the VC additive on the mechanical stability of the CEI film, SEM characterization was performed on the cathodes of the half-cells with PE and PE1VC electrolytes after 300 cycles at 10 C. As shown in Figure 5A-C, the NFM@CTA-4 particles in the PE electrolyte exhibit degraded morphological regularity, with visible surface cracks, indicative of severe structural degradation. In contrast,

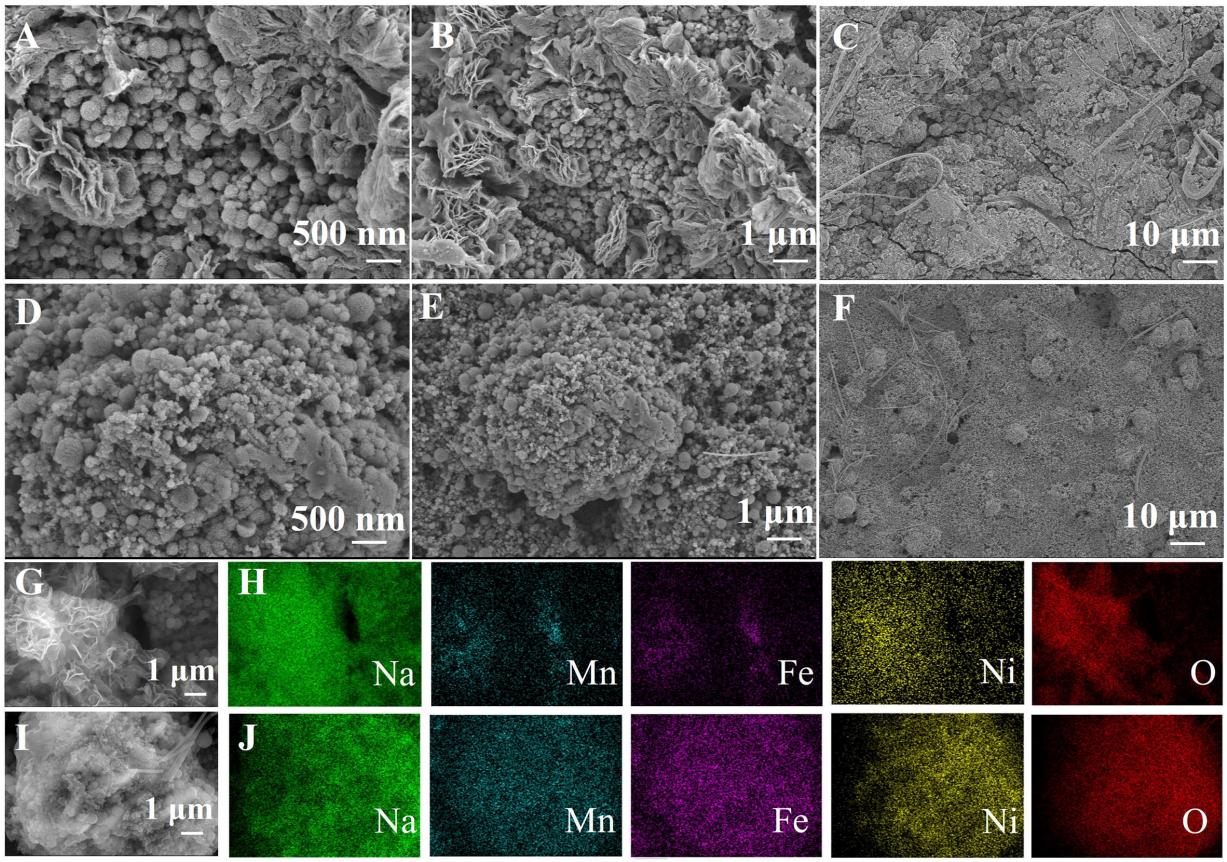

Figure 5. SEM images of the NFM@CTA-4 cathode after 300 cycles at 10 C in PE (A-C) and PE1VC (D-F). SEM images and corresponding EDS elemental mappings of the cycled cathodes in PE (G and H) and PE1VC (I and J) (scale bars in G-J: 1 μm).

the cathode cycled in the PE1VC electrolyte [Figure 5D-F] demonstrates substantially improved structural integrity, with virtually no surface cracks and a more uniform, densely packed particle distribution. This observation suggests that the VC additive enables the formation of a mechanically robust CEI film that effectively preserves the structural integrity of the cathode particles. Such a robust CEI film not only promotes homogeneous and stable electrode reactions but also suppresses electrolyte decomposition. Additionally, the EDS [Figure 5G-J] and quantitative elemental analyses [Supplementary Tables 1 and 2] indicate that the Na content in the CEI film of the PE-based electrode is higher than that in the PE1VC-based electrode. This difference is attributed to the more serious accumulation of electrolyte decomposition products on the cathode surface in the baseline PE electrolyte during cycling, which impedes Na^+ transport and promotes interfacial Na^+ accumulation[43]. Moreover, distinct morphological evolutions were observed after 300 cycles. In our previous work, the NFM@CTA-4 cathode exhibited a spherical morphology[26]. In contrast, the NFM@CTA-4 electrode developed a flower-like microstructure after cycling in the PE-based electrolyte, indicating severe structural degradation. However, the PE1VC-based electrode retained its original spherical morphology, reflecting exceptional structural integrity. The morphological differences between PE and PE1VC are mainly due to the VC additive, which facilitates the formation of a chemically stable CEI film, thereby suppressing morphological degradation under attack by electrolyte decomposition products. As a result, the cathode exhibited outstanding cycling stability at high rates and elevated temperatures.

This study demonstrates that the synergistic electrolyte strategy effectively enhances electrochemical performance in Na-metal half-cells. Admittedly, Na-metal half-cells face substantial challenges in practice, including continuous electrolyte decomposition, dendritic sodium deposition, and anodic overpotential drift

[44]. In contrast, full cells based on relatively stable anodes (e.g., hard carbon) offer significantly improved interfacial stability and suppressed parasitic side reactions[45], offering greater promise for practical implementation. Thus, future investigations should extend this synergistic electrolyte engineering strategy to full-cell configurations, particularly under industrially representative conditions, such as high areal loadings of active materials.

CONCLUSION

This work proposed a synergistic electrolyte engineering strategy based on a PC/EMC/FEC/VC system to enhance the cycling stability of the LTMO-based SIBs under high-rate and elevated-temperature conditions. The PC/EMC binary solvent optimizes Na^+ solvation energy, and the FEC additive facilitates the formation of a stable, ionically conductive SEI film on the Na anode, collectively improving rate capability and cycling stability. Additionally, the VC additive, with its lower LUMO and higher HOMO energy levels, promotes the rapid formation of a CEI film that is chemically, thermally, and mechanically robust. Consequently, the NFM@CTA-4||Na half-cells delivered an initial capacity of 80 mAh g^{-1} at 10 C (from the long-term cycling test) and maintained 62.7 mAh g^{-1} (78.4 % retention) after 600 cycles at 10 C. It showed 94.4 mAh g^{-1} at 10 C and maintained 54.8 mAh g^{-1} after 300 cycles at 1 C at 90 °C. This scientific synergistic electrolyte design provides critical guidance for developing high-stability LTMO-based SIBs, accelerating their practical deployment for outdoor stationary energy storage.

DECLARATIONS

Authors' contributions

Methodology, investigation, formal analysis, data visualization, and writing-original draft: Zhao, Z.; Wang, T.; Yang, Z.

Formal analysis and investigation: Wang, X.; Cai, Y.

Review, supervision, and funding acquisition: Zhao, Z.; Lu, J.; Chen, W.

Availability of data and materials

The original contributions presented in this study are included in the article/Supplementary Materials.

AI and AI-assisted tools statement

Not applicable.

Financial support and sponsorship

This work was supported by the HJ Program Research Funding Support from the National Natural Science Foundation of China [Grant No. 24210005-N]; Zhejiang Provincial Natural Science Foundation of China [Grant No. LQN26B030009]; Science Foundation of Zhejiang Sci-Tech University [Grant Nos. 23212091-Y and 24212217-Y]; the "Pioneer" and "Leading Goose" R&D Program of Zhejiang Province of China [No. 2024C01056].

Conflicts of interest

Zhao, Z. and Lu, J. are Guest Editors of the Special Issue "High-Safety Rechargeable Batteries: Material, Interface, Mechanism, and Performance" in *Energy Materials* and were not involved in any steps of the editorial process, including reviewer selection, manuscript handling, or decision-making, while the other authors have declared that they have no conflicts of interest.

Ethical approval and consent to participate

Not applicable.

Consent for publication

Not applicable.

Supplementary Materials

Supplementary Materials

REFERENCES

1. Zhao, Z.; Hou, N.; Hong, Z.; Ming, S.; Lu, J.; Chen, W. Kinetic insights for high-rate and low-temperature ammonium-ion batteries/supercapacitors. *Energy. Storage. Materi.* **2025**, *81*, 104539. DOI
2. Ortiz-Vitoriano, N.; Drewett, N. E.; Gonzalo, E.; Rojo, T. High performance manganese-based layered oxide cathodes: overcoming the challenges of sodium ion batteries. *Energy. Environ. Sci.* **2017**, *10*, 1051-74. DOI
3. Kubota, K.; Komaba, S. Review—practical issues and future perspective for Na-ion batteries. *J. Electrochem. Soc.* **2015**, *162*, A2538-50. DOI
4. Weldegebrieal, G. K.; Tangthuam, P.; Lao-Ian, W.; et al. Sodium-ion batteries: from conventional to anode-free configurations: materials, mechanisms, and future prospects. *J. Energy. Storage.* **2025**, *135*, 118386. DOI
5. Liu, Q.; Hu, Z.; Chen, M.; et al. The cathode choice for commercialization of sodium-ion batteries: layered transition metal oxides versus prussian blue analogs. *Adv. Funct. Mater.* **2020**, *30*, 1909530. DOI
6. Liu, Q.; Hu, Z.; Chen, M.; et al. Recent progress of layered transition metal oxide cathodes for sodium-ion batteries. *Small* **2019**, *15*, 1805381. DOI
7. Dai, P.; Shi, C.; Huang, Z.; et al. A new film-forming electrolyte additive in enhancing the interface of layered cathode and cycling life of sodium ion batteries. *Energy. Storage. Mater.* **2023**, *56*, 551-61. DOI
8. Wang, J.; Zhu, Y.; Su, Y.; et al. Routes to high-performance layered oxide cathodes for sodium-ion batteries. *Chem. Soc. Rev.* **2024**, *53*, 4230-301. DOI
9. Zhou, L.; Wang, H.; Cao, L.; et al. Synergetic phase transition suppression and air-stability engineering in layered cathode materials for sodium ion batteries. *Chem. Eng. J.* **2025**, *526*, 170700. DOI
10. Takada, K.; Yamada, Y.; Watanabe, E.; et al. Unusual passivation ability of superconcentrated electrolytes toward hard carbon negative electrodes in sodium-ion batteries. *ACS. Appl. Mater. Interfaces.* **2017**, *9*, 33802-9. DOI
11. Lu, H.; Chen, X.; Jia, Y.; et al. Engineering Al_2O_3 atomic layer deposition: enhanced hard carbon-electrolyte interface towards practical sodium ion batteries. *Nano. Energy.* **2019**, *64*, 103903. DOI
12. Jo, J. H.; Choi, J. U.; Konarov, A.; et al. Sodium-ion batteries: building effective layered cathode materials with long-term cycling by modifying the surface via sodium phosphate. *Adv. Funct. Mater.* **2018**, *28*, 1705968. DOI
13. Lin, Y.; Jin, X.; Gao, S.; et al. Improved interface construction on anode and cathode for Na-ion batteries using ultralow-concentration electrolyte containing dual-additives. *Chem. A. Eur. J.* **2024**, *30*, e202303741. DOI
14. Jayakumar, R.; Chak, C. M.; Shipitsyn, V.; et al. Ethylene sulfate-enabled stable interphases in fluorinated ether electrolytes for high-performance sodium-ion batteries. *J. Power. Sources.* **2026**, *662*, 238753. DOI
15. Ponrouch, A.; Marchante, E.; Courty, M.; Tarascon, J.; Palacín, M. R. In search of an optimized electrolyte for Na-ion batteries. *Energy. Environ. Sci.* **2012**, *5*, 8572. DOI
16. Wang, S.; Zhang, J.; Hua, W.; et al. Solvation-enhanced electrolyte on layered oxide cathode tailoring even and stable CEI for durable sodium storage. *Carb. Neutr.* **2023**, *2*, 20. DOI
17. Zhou, Z.; Qian, Y.; Gao, J.; et al. A nonflammable carbonate-phosphate hybrid electrolyte enabling high-temperature sodium-ion full batteries. *Energy. Storage. Mater.* **2026**, *89*, 105229. DOI
18. Li, Q.; Jiao, S.; Luo, L.; et al. Wide-temperature electrolytes for lithium-ion batteries. *ACS. Appl. Mater. Interfaces.* **2017**, *9*, 18826-35. DOI
19. Fu, J.; Li, S.; Luo, C.; et al. Design principles for fluoroethylene carbonate additive-electrode compatibility in nanoporous sugarcane bagasse-based hard carbon sodium ion anodes. *J. Mater. Chem. A.* **2026**, *14*, 10929-39. DOI
20. Huang, J.; Liu, J.; He, J.; et al. Optimizing electrode/electrolyte interphases and Li-ion flux/solvation for lithium-metal batteries with qua-functional heptafluorobutyric anhydride. *Angew. Chem. Int. Ed.* **2021**, *60*, 20717-22. DOI
21. Tiwari, R.; Kumar, D.; Verma, D. K.; et al. Fundamental chemical and physical properties of electrolytes in energy storage devices: a review. *J. Energy. Storage.* **2024**, *81*, 110361. DOI
22. Bouguern, M. D.; M R, A. K.; Zaghib, K. The critical role of interfaces in advanced Li-ion battery technology: a comprehensive review. *J. Power. Sources.* **2024**, *623*, 235457. DOI
23. Chang, M.; Cheng, F.; Zhang, W.; et al. Antioxidant layer enables chemically stable cathode-electrolyte interface towards durable and safe Li-ion batteries. *Energy. Storage. Mater.* **2023**, *61*, 102872. DOI
24. Wu, D.; Zhu, C.; Wang, H.; et al. Mechanically and thermally stable cathode electrolyte interphase enables high-temperature, high-voltage Li||$LiCoO_2$ batteries. *Angew. Chem. Int. Ed.* **2024**, *63*, e202315608. DOI

25. Cheng, H.; He, Y. Temperature-dependent evolution of the CEI on graphite electrodes and its impact on dual-ion battery performance. *Chem. Phys. Lett.* **2026**, *889*, 142711. DOI
26. Yang, Z.; Liu, F.; Yu, T.; et al. Performance improvement of O3-type $Na(NiFeMn)_{1/3}O_2$ cathodes by tannic acid-derived carbon coating. *J. Electroanal. Chem.* **2025**, *990*, 119182. DOI
27. Goodenough, J.; Kim, Y. Challenges for rechargeable batteries. *J. Power. Sources.* **2011**, *196*, 6688-94. DOI
28. Kondou, S.; Sakashita, Y.; Morinaga, A.; et al. Concentrated nonaqueous polyelectrolyte solutions: high Na-ion transference number and surface-tethered polyanion layer for sodium-metal batteries. *ACS. Appl. Mater. Interfaces.* **2023**, *15*, 11741-55. DOI
29. Xia, B.; Ye, B.; Cao, J. Polarization voltage characterization of lithium-ion batteries based on a lumped diffusion model and joint parameter estimation algorithm. *Energies* **2022**, *15*, 1150. DOI
30. Adebanjo, I. T.; Eko, J.; Agbeyegbe, A. G.; et al. A comprehensive review of lithium-ion battery components degradation and operational considerations: a safety perspective. *Energy. Adv.* **2025**, *4*, 820-77. DOI
31. Dai, H.; Gomes, L.; Maxwell, D.; et al. Exploring the role of an electrolyte additive in suppressing surface reconstruction of a Ni-rich NMC cathode at ultrahigh voltage via enhanced in situ and operando characterization methods. *ACS. Appl. Mater. Interfaces.* **2024**, *16*, 8639-54. DOI PubMed PMC
32. Shi, J.; Ding, L.; Wan, Y.; et al. Achieving long-cycling sodium-ion full cells in ether-based electrolyte with vinylene carbonate additive. *J. Energy. Chem.* **2021**, *57*, 650-5. DOI
33. Kubot, M.; Balke, L.; Scholz, J.; et al. High-voltage instability of vinylene carbonate (VC): impact of formed poly-VC on interphases and toxicity. *Adv. Sci.* **2023**, *11*, 2305282. DOI PubMed PMC
34. Lee, W. J.; Prasanna, K.; Jo, Y. N.; Kim, K. J.; Kim, H. S.; Lee, C. W. Depth profile studies on nickel rich cathode material surfaces after cycling with an electrolyte containing vinylene carbonate at elevated temperature. *Phys. Chem. Chem. Phys.* **2014**, *16*, 17062-71. DOI PubMed
35. Ota, H.; Sakata, Y.; Inoue, A.; Yamaguchi, S. Analysis of vinylene carbonate derived SEI layers on graphite anode. *J. Electrochem. Soc.* **2004**, *151*, A1659. DOI
36. Yu, Y.; Ning, D.; Li, Q.; et al. Revealing the anionic redox chemistry in O3-type layered oxide cathode for sodium-ion batteries. *Energy. Storage. Mater.* **2021**, *38*, 130-40. DOI
37. Liu, K.; Tan, S.; Moon, J.; et al. Insights into the enhanced cycle and rate performances of the F-substituted P2-type oxide cathodes for sodium-ion batteries. *Adv. Energy. Mater.* **2020**, *10*, 2000135. DOI
38. Li, H.; Ma, Q.; Yuan, Y.; et al. Mesoporous N,S-rich carbon hollow nanospheres controllably prepared from poly(2-aminothiazole) with ultrafast and highly durable potassium storage. *Adv. Funct. Mater.* **2023**, *34*, 2301987. DOI
39. Ghasemiahangarani, P.; Farhan, G.; Del, Mundo. D.; Schoetz, T. Charge storage mechanisms in batteries and capacitors: a perspective of the electrochemical interface. *Adv. Energy. Mater.* **2024**, *15*, 2404704. DOI
40. Eum, D.; Kim, B.; Song, J.; et al. Coupling structural evolution and oxygen-redox electrochemistry in layered transition metal oxides. *Nat. Mater.* **2022**, *21*, 664-72. DOI
41. Yu, R.; Wang, C.; Duan, H.; et al. Manipulating charge-transfer kinetics of lithium-rich layered oxide cathodes in halide all-solid-state batteries. *Adv. Mater.* **2022**, *35*, 2207234. DOI
42. Lee, Y.; Lee, J.; Kim, H.; Kang, K.; Choi, N. Highly stable linear carbonate-containing electrolytes with fluoroethylene carbonate for high-performance cathodes in sodium-ion batteries. *J. Power. Sources.* **2016**, *320*, 49-58. DOI
43. Chen, G.; Ya, Y.; Li, Y.; et al. Stabilizing high-voltage operation of layered oxide cathodes through ionic interdiffusion-triggered surface reinforcement for sodium-ion batteries. *J. Energy. Chem.* **2026**, *116*, 409-20. DOI
44. Singla, A.; Naik, K. G.; Vishnugopi, B. S.; Mukherjee, P. P. Heterogeneous solid electrolyte interphase interactions dictate interface instability in sodium metal electrodes. *Adv. Sci.* **2024**, *11*, 2404887. DOI PubMed PMC
45. Yang, H.; Zeng, Y.; Li, W.; Yang, Y.; Zhao, J. The importance of fabricating hard carbon-based full cells to overcome sodium metal anode limitations in evaluating high-mass-loading cathodes. *ACS. Energy. Lett.* **2025**, *10*, 2868-76. DOI